Orientation and Path Dependence of Formability in the Stress- and the Extended Stress-Based Forming Limit Curves

C. Hari Manoj Simha
e-mail: simha@lagavulin.uwaterloo.ca

Kaan Inal

Michael J. Worswick
e-mail: worswick@lagavulin.uwaterloo.ca

Department of Mechanical and Mechatronics Engineering,
University of Waterloo,
Waterloo, ON, N2L 3G1, Canada

*This article analyzes the formability data sets for aluminum killed steel (Laukonis, J. V., and Ghosh, A. K., 1978, "Effects of Strain Path Changes on the Formability of Sheet Metals," Metall. Trans. A., **9**, pp. 1849–1856), for Al 2008-T4 (Graf, A., and Hosford, W., 1993, "Effect of Changing Strain Paths on Forming Limit Diagrams of Al 2008-T4," Metall. Trans. A, **24A**, pp. 2503–2512) and for Al 6111-T4 (Graf, A., and Hosford, W., 1994, "The Influence of Strain-Path Changes on Forming Limit Diagrams of Al 6111 T4," Int. J. Mech. Sci., **36**, pp. 897–910). These articles present strain-based forming limit curves (ϵFLCs) for both as-received and prestrained sheets. Using phenomenological yield functions, and assuming isotropic hardening, the ϵFLCs are transformed into principal stress space to obtain stress-based forming limit curves (σFLCs) and the principal stresses are transformed into effective stress and mean stress space to obtain the extended stress-based forming limit curves (XSFLCs). A definition of path dependence for the σFLC and XSFLC is proposed and used to classify the obtained limit curves as path dependent or independent. The path dependence of forming limit stresses is observed for some of the prestrain paths. Based on the results, a novel criterion that, with a knowledge of the forming limit stresses of the as-received material, can be used to predict whether the limit stresses are path dependent or independent for a given prestrain path is proposed. The results also suggest that kinematic hardening and transient hardening effects may explain the path dependence observed in some of the prestrain paths.*
[DOI: 10.1115/1.2931152]

1 Introduction

The strain-based forming limit curve (ϵFLC), introduced by Keeler and Backofen [1], can be used to predict the onset of necking in sheet metal forming for load paths that are proportional in strain space. Here, the load paths are due to in-plane loads. However, for load paths that are nonproportional, ϵFLCs cannot be used. For example, Graf and Hosford [2] prestrained sheets of Al 2008 aluminum alloy and found that the ϵFLCs of the prestrained sheets shifted and changed shape when compared with the ϵFLC of the as-received sheet. Similar results were obtained for aluminum killed steel sheet by Laukonis and Ghosh [3] and Al 6111 sheets by Graf and Hosford [4].

Stress-based forming limit curves (σFLCs) have been suggested as an alternative to the ϵFLCs [5–7]. Stoughton [8] made suitable constitutive assumptions and transformed the ϵFLCs of the prestrained and the as-received sheets into principal stress space. He showed that, in most cases, the stress-based limit curves were nearly coincidental. That is, within the scope of the constitutive assumptions and experimental uncertainty, there is one limit curve in principal stress space that can be used to predict the onset of necking in sheet metal during in-plane proportional load paths as well as nonproportional paths. Stated alternatively, FLCs in principal stress space may be path independent. Subsequently, Stoughton [9] addressed the criticism that the ϵFLCs collapsed into nearly coincidental curves because of the saturation of the stress levels in the stress-strain curve used to transform the strain-based FLCs. He showed that when the ϵFLC was shifted by about 10%, the forming limit stresses changed by about 5 MPa. Likewise, Sakash et al. [10] analyzed the data of Graf and Hosford [2] and showed that when the ϵFLC was shifted by 5% the limit stresses changed by 1.5%. That is, they showed that the limit stresses had not saturated. See also Refs. [11,12] for arguments, along similar lines, against the critique of the saturation of limit stresses.

The property of path independence make FLCs in terms of stresses attractive and consequently the property has received attention. Chow and Yang [13] have examined the Al 2008 data of Graf and Hosford by using a model that combined anisotropy of strength and isotropic and kinematic hardening and concluded that the prestrained σFLCs did not converge with that of the as-received material when the prestrains were large. Wu et al. [14] adopted a crystal plasticity-based model in conjunction with the Marciniak and Kuczynski (MK) [15] approach and concluded that the σFLCs were less path dependent when compared to the ϵFLCs. It is worth noting that they pointed out that the presence of sufficiently large prestrains renders the σFLCs path dependent. Yoshida et al. [12] carried out theoretical analyses using the MK approach and nonproportional loading paths. Path independence was observed in the load paths that included unloading, while forming limit stresses were path dependent for load paths that involved a change in the loading direction without unloading.

Other studies of stress-based forming limits have focused on theoretical, experimental, and orientation dependences of formability. Starting with the ϵFLC, Stoughton and Zhu [11] carried out instability analyses and demonstrated path independence of the σFLC. Recently, Sakash et al. [10] have used the σFLCs to predict failure in finite element computations of the dome height experiment; and the computational predictions were found to be in

Contributed by the Materials Division of ASME for publication in the JOURNAL OF ENGINEERING MATERIALS AND TECHNOLOGY. Manuscript received August 10, 2007; final manuscript received February 22, 2008; published online September 17, 2008. Assoc. Editor: Yanyao Jiang.

good agreement with the experimental results. Furthermore, Stoughton and Yoon [16] have considered the orientation dependence of formability in the context of σFLCs.

The ϵFLCs and the σFLCs are intended for use under in-plane loading and cannot be used for processes such as hydroforming without some consideration for the triaxial state of loading. During hydroforming, as the tube expands and contacts the die, a combination of the through-thickness compressive stress due to the internal fluid pressure and frictional forces at the tube-die interface causes the neck to initiate under a three-dimensional state of stress. A discussion of the phenomenology of necking in hydroforming can be found in the article by Simha et al. [17]; this article is hereafter referred to as Article I. In this article, they proposed a new FLC, the extended stress-based forming limit curve (XSFLC), which is obtained by transforming the σFLC into the invariants effective stress and mean stress. Effective stress is defined in accord with the choice of the yield function used in the constitutive description and mean stress is one-third of the trace of the stress tensor. These invariants, computed assuming J_2 flow theory and isotropic hardening, can accommodate three-dimensional stress states. The XSFLC is primarily intended to predict localization under three-dimensional loading. However, it can also be used for situations wherein the neck forms under in-plane loading of the sheet. In a forthcoming publication, Simha et al. [18] demonstrated using stretch flange forming experiments that the XSFLC can also be used in situations where the neck forms under in-plane loading.

Four assumptions were made in order to be able to use the XSFLC to predict the onset of necking during hydroforming and these are itemized below using the same numbering scheme as in Article I.

1. Isotropic hardening and J_2 flow theory were assumed to transform the ϵFLC into the σFLC and the XSFLC.
2. The effective stress and mean stresses in the XSFLC are valid only for in-plane loading, since the ϵFLC is measured under in-plane loading. However, in Article I, these effective stresses and mean stresses were assumed to be equivalent to the effective stresses and mean stresses that develop in necks that form under three-dimensional loading.
3. During tube bending, the outside of the tube is subjected to tension (primary loading) along the long axis of the tube. Subsequently, during hydroforming, it is subjected to tension (secondary loading) along a direction that is approximately perpendicular to the direction of loading during bending. The primary and secondary load paths are designated as tension-tension. In Article I, when the stress-based approach was used to predict necking, path dependence was observed in those portions of the prebent tubes subjected to tension-tension paths. To fix this idea, consider Fig. 1, where a schematic of the XSFLC (effective stress, Σ_{eq}, versus mean stress, Σ_{hyd}) is shown. The left edge corresponds to uniaxial loading, the right to equibiaxial tensile loading, and the dip in the middle to plane-strain loading. During bending, the outside of the tube will follow path *ou*, where initial yielding of the tube will occur when the effective stress exceed Σ_0 (yield surfaces are horizontal lines in XSLFC space) and the effective strains of about 25% in the 90 deg bend, for a 76 mm diameter tube, can be attained at the terminal point *u*. The level of hardening at the terminus of the load path is Σ_p. A neck will not be formed along this path as it does not intersect with the XSFLC. The material is unloaded along this path and reloaded along *os* during hydroforming and the onset of necking is not when the load path *os* intersects the as-received XSFLC, but when it intersects the yield surface Σ_p. That is, during the secondary load path, necking succeeds yielding. The formability of a material element that has attained a hardening level Σ_p during primary loading was assumed to be $\max[\Sigma_p, \Sigma_{XSFLC}]$. The path *ob* in Fig. 1 will be discussed in a later section.

   The experimental evidence to support this assumption is equivocal. This assumption has been shown to be correct in the case of aluminum tubes [19]. For steel tubes, on the other hand, Yoshida et al. [12] have found that this assumption does not hold in all cases of nonproportional loading. Therefore, for the XSFLC approach, it is taken to be an assumption.
4. In addition to the path dependence observed in tension-tension paths, path dependence was also observed along compression-tension paths. During bending, the portions of the tube in the inside of the bend will be subjected to compression, and subsequently subjected to tension during hydroforming. This path dependence was circumvented in Article I using a purely arbitrary approach and further details about this assumption can be found in the article.

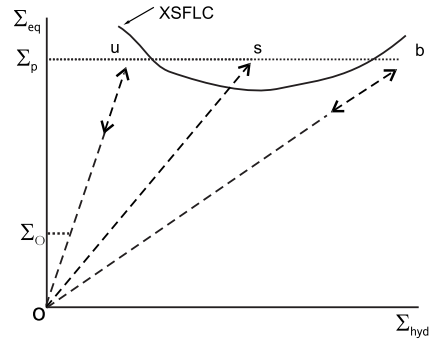

Fig. 1 Schematic illustrating Assumption 3. Primary loading path may be along uniaxial path *ou* or equibiaxial path *ob*. Initial yielding is at Σ_0, and the hardening at the terminal point of the primary path is Σ_p. No necking occurs when the secondary load path, *os*, intersects the as-received XSFLC, but necking occurs when yielding occurs at point *s*.

The centerpiece of the XSFLC approach is Assumption 2, and it is studied using a computational approach by Simha et al. [20]. In the current work, Assumptions 1 and 3 are examined. Isotropy of strength was assumed in Article I, and this precludes the description of the orientation dependence of formability for textured sheet. In the current work, the incorporation of anisotropy of formability is studied. In addition, Assumption 3 used to circumvent the path dependence observed in tension-tension load paths, as described above, is also examined. To this end, the well known formability data sets of Graf and Hosford [2], Graf and Hosford [4], and Laukonis and Ghosh [3] are analyzed using phenomenological plasticity models. A working definition of path dependence is presented and used to demonstrate that there is indeed a path dependence in the stress-based framework, and it is demonstrated that Assumption 3 of the XSFLC approach allows a simple way to circumvent this path dependence in some instances. Furthermore, a novel criterion that can be used to predict the onset of path dependence is also presented.

By way of terminology, the term stress-based approach implies both σFLCs and XSFLCs and forming limit stresses imply stresses in the rolling direction (RD) and the transverse directions (TD).

2 Constitutive Descriptions

This section presents brief descriptions of the constitutive models used in the analyses of the formability data. In what follows, x and y are taken to be parallel to the RD and TD, and z the direction normal to the plane of the sheet.

2.1 Barlat–Lian Yield Function. The yield function due to

Table 1 KB yield function parameters for Al2008, Al6111, and steel

	L_{11}	L_{22}	L_{33}	L_{12}	L_{13}	L_{23}	L_{66}	B_1	B_2	B_3	c
Al2008[a]	0.6667	0.6875	0.6945	−0.3298	−0.3368	−0.3577	0.9763	$0.017\bar{Y}$	$-0.001\bar{Y}$	$-0.016\bar{Y}$	0.2
Al6111[b]	0.6667	0.6873	0.6203	−0.3668	−0.2998	−0.3205	1.0144	$-0.0029\bar{Y}$	$-0.05\bar{Y}$	$0.0529\bar{Y}$	0.15
Steel[c]	0.6667	0.6436	0.5226	−0.3938	−0.2727	−0.2498	1.0145	$0.003\bar{Y}$	$-0.01\bar{Y}$	$-0.007\bar{Y}$	0.1

[a] $m=8$ and $\bar{Y}=153+(390-153)[1-\exp(-8\bar{\epsilon})]$.

[b] $m=8$ and $\bar{Y}=561\bar{\epsilon}^{0.252}$.

[c] $m=6$ and $\bar{Y}=501\bar{\epsilon}^{0.242}$.

Barlat and Lian (BL) [21] can be used to model anisotropy of sheet metal for plane-stress states and it is given by

$$\phi = a|\sigma_x|^m + a|h\sigma_y|^m + (2-a)|\sigma_x - h\sigma_y|^m = 2\bar{Y}^m \tag{1}$$

where a and h are material parameters. The exponent m is 8 for fcc materials and 6 for bcc materials as per the suggestion of Hosford [22]. In the above equation, $\bar{Y}$ is the hardening response, which is expressed as a function of the effective plastic strain. The two material parameters can be calibrated using either yield strength measurements made at three angles to the rolling direction (RD) σ_0, σ_{45}, and σ_{90}, or by using the Lankford coefficients R_0, R_{45}, and R_{90}. The calibration of this model is discussed by BL [21] and the equations used to transform the ϵFLCs into σFLCs using this yield function can be found in the article by Sakash et al. [10].

2.2 Karafillis–Boyce Yield Function. In this work, the yield function due to Karafillis and Boyce (KB) [23] is used to transform the ϵFLCs into principal stress space, and this section presents a brief description of this yield function. A thorough treatment can be found in the articles by KB [23] and Cao et al. [24]. Boldface Latin and Greek letters are used to denote tensor fields. Let the stress tensor field in the anisotropic body be $\boldsymbol{\sigma}$. A traceless and symmetric fourth order transformation tensor $\boldsymbol{L}$ is used to transform the stress tensor in the anisotropic body into an isotropic plasticity equivalent (IPE) body as

$$\boldsymbol{S} = \boldsymbol{L}(\boldsymbol{\sigma} - \boldsymbol{B})$$

where $\boldsymbol{B}$ is the traceless backstress used to offset the yield function to describe differences in yielding due to tension and compression. $\boldsymbol{S}$ is the IPE deviatoric stress tensor. The tensor $\boldsymbol{L}$ transforms the stresses acting on the anisotropic body to obtain the stresses acting on the equivalent isotropic body. It bears emphasis that $\boldsymbol{B}$ is used to represent a strength differential effect and not used as a kinematic hardening variable. The KB yield function is obtained by mixing two functions ϕ_1 and ϕ_2 that are functions of the principal values of $\boldsymbol{S}$ through a weighting factor c whose value is $0<c<1$. The KB model functions are

$$\phi = (1-c)\phi_1 + c\phi_2 = 2\bar{Y}^m$$

$$\phi_1 = |S_1 - S_2|^m + |S_2 - S_3|^m + |S_3 - S_1|^m$$

$$\phi_2 = \frac{3^m}{2^{m-1}+1}[|S_1|^m + |S_2|^m + |S_3|^m] \tag{2}$$

where m is the exponent whose value lies between 2 and ∞, and $\bar{Y}$ is the hardening curve expressed as a function of the equivalent plastic strain. The symmetric part of the velocity gradient, $\boldsymbol{D}^p$, of the *anisotropic body* can be computed from

$$\boldsymbol{D}^p = \boldsymbol{L}\boldsymbol{d}^p = \boldsymbol{L}d\lambda\frac{\partial\phi}{\partial\boldsymbol{S}} \tag{3}$$

where the associated flow rule has been used to compute the velocity gradient of the isotropic body and $d\lambda$ is the plastic multiplier, and $\boldsymbol{d}^p$ is the plastic work conjugate of $\boldsymbol{S}$. The foregoing equation is a consequence of assuming equality of plastic work dissipation in the isotropic and anisotropic bodies KB [23] and Cao et al. [24]. The KB model equations, and calibration of the model parameters for in-plane loading of sheet metal are discussed in Appendix B and the model parameters for aluminum killed steel, Al 2008-T4 and Al 6111-T4, are shown in Table 1. Figure 2 presents plots of yield strength, Lankford coefficients, and yield contours for the three materials and these were obtained using the KB model.

3 Working Definition of Path Independence

Path independence of the stress-based FLC implies that, within the scope of the constitutive assumption, there exists one curve in principal stress space, derived from the as-received ϵFLC, that can be used to predict the onset of necking under linear as well as nonlinear load paths. This implication applies to the XSFLCs as well. Yoshida et al. [12] have defined the path independence in their theoretical study to be $(\sigma_{11}^P - \sigma_{11}^C)/\sigma_{11}^P$, where σ_{11}^P is the forming limit stress for linear paths and σ_{11}^C is the limit stress for nonlinear paths. If the above quantity was less than $\pm 1\%$, path independence was assumed. This definition, although admissible in a theoretical study, is too restrictive since it does not take into account the uncertainties associated with the measurement of the as-received ϵFLC and those associated with the derivation of the σFLC and XSFLC.

The σFLC and the XSFLC depend on the uncertainty of the strain measurements in the as-received ϵFLC, uncertainty due to statistical distribution of defects, the constitutive model used to derive them, and the stress-strain response used in the transformation to stress space. It is well known that the uncertainty associated with the ϵFLC can be as high as 2%, especially when the circle-grid method is used to measure the strains. Strain-based FLCs with uncertainties lower than 2% can be obtained using optical techniques. The statistical distribution of defects also influences the uncertainties associated with the necking strain. A larger defect density will lead to lower necking strains and vice versa. The uncertainty in necking strain associated with the statistical nature of defects may be higher than 2%.

There is also an uncertainty associated with the stress-strain curve used in transforming the as-received ϵFLC into the σFLC. Multiaxial tests can be used to obtain the stress-strain response for transforming the ϵFLCS. Koc et al. [25], for example, discussed and contrasted the various techniques that can be used to evaluate the stress-strain response for sheet metal. In practice, however, the tensile stress-strain curve obtained using the E-8 ASTM standard for sheet metal testing is used for this purpose. The onset of localization in these tests limits the strain range over which the stress-strain response is valid, which is approximately 20–30% for conventional engineering alloys. This implies that the tensile stress-strain curve has to be extrapolated to transform the ϵFLC into the σFLC, thereby introducing an uncertainty into the σFLC.

Finally, there is an uncertainty associated with the constitutive model used to transform the ϵFLC into the σFLC. Articles by Stoughton [8], Sakash et al. [10], and Stoughton and Yoon [16] address the dependence of the σFLC on the constitutive model

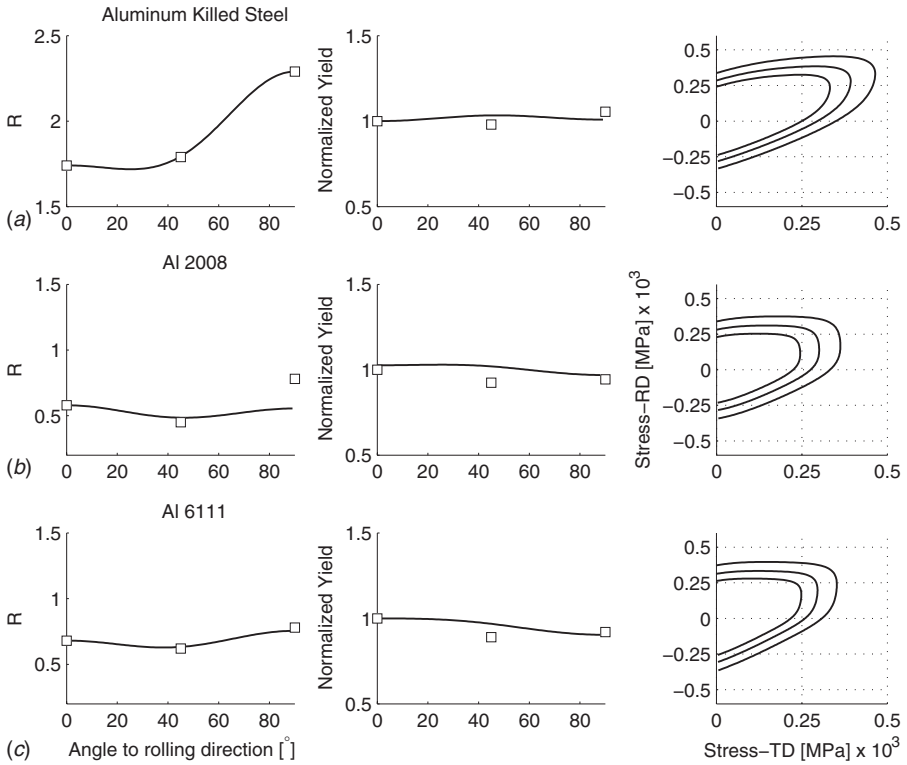

Fig. 2 Variation of Lankford coefficients and yield strength to the RD and yield loci at 5%, 10%, and 20%. (*a*) Aluminum killed steel, (*b*) Al 2008, and (*c*) Al 6111.

used. In this context, it is worthwhile to emphasize the observation of Stoughton and Zhu [11] that "…the only requirement for the successful application of a stress-based FLD analysis is that one must use the same material model with the same material parameters in the finite element modeling (FEM) analysis or calculations in tryout or in the stamping plant as are used in the original calculation of the stress-based FLC."

From the foregoing, it can be seen that there is considerable difficulty in identifying the uncertainty associated with the σFLC and the XSFLC obtained from the as-received ϵFLC. Nevertheless, these uncertainties will have to be factored into any quantitative definition of path independence.

In this work, it is assumed that the uncertainty associated with the as-received ϵFLC is 2%. For example, the actual strain at the onset of necking will lie between the ordered pair $(\epsilon_2 \pm 0.02, \epsilon_1 \pm 0.02)$, where the ϵ_i is the measurement. If the upper bound and lower bound ϵFLCs are transformed into principal stress space, the corresponding upper bound and lower bound stress-based limit curves will be separated by less than 2%. Therefore, in order to account for uncertainties other than those associated with the ϵFLC, the uncertainty in the σFLC is also taken to be 2%; likewise for the XSFLC.

Since uncertainty has been accounted for, path independence is defined as illustrated in Fig. 3. Schematics of the stress-based FLCs for the as-received and prestrained sheet are shown in Fig. 3(*a*). Notice that the span of the curve in the minor principal direction may not be the same as the span of the as-received curve. Therefore, it is difficult to develop a definition of path independence except in some limited cases. Since 80% of necking in metal forming processes occurs at or near the plane-strain limit, the definition of path independence centers around the plane-strain region of the FLC. The difference, at the plane-strain region, between the as-received and prestrained curves is designated as Δ in the figure, where Δ is normalized with stress from the plane-strain region of the as-received curve. Since there is an uncertainty of 2% associated with the as-received curve as well as the prestrained curve, the magnitude of Δ is taken to be the root mean square of these uncertainites. That is, $\Delta \approx 3\%$. If the magnitude of Δ is below 3%, the stress-based FLC of the prestrained material is taken to be path independent. When $\Delta > 3\%$, the σFLC of the prestrained curve is path dependent. Note that there is a possibility that outside of the plane-strain region the difference between the

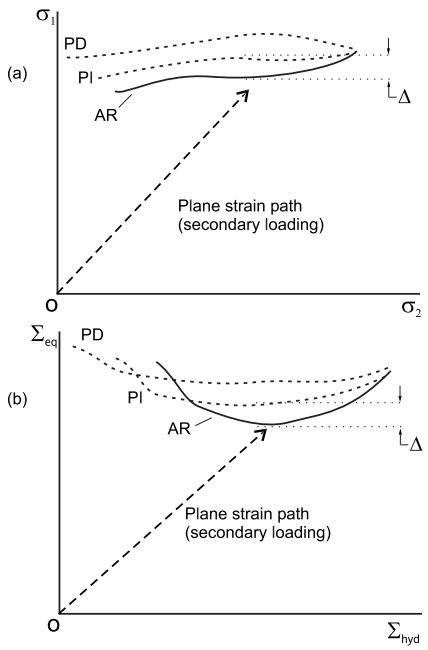

Fig. 3 Schematic illustrating definition of path dependence. Path dependence is assumed if Δ is less than ≈3%. PI—path independent, PD—path dependent, and AR—as-received.

as-received and prestrained curves may be greater than 3%, while it is less than 3% at the plane-strain region; nevertheless, the prestrained limit curve is taken to be path independent.

It is worth pointing out that 3% in stress space transforms into higher values in strain space. For instance, in the AL6111 data considered in this work, a 3% uncertainty of the stress at the plane-strain portion of the FLC transforms into approximately 12% in strain space.

In practice, the most accurate portion of the ϵFLC is around the plane-strain region. The farther the necking strains are from the plane-strain portion, the higher the associated uncertainty. This feature provides support for our definition of path independence. However, even at the plane-strain portion, since only one measurement may be taken as in some of the Graf and Hosford [12] data, the uncertainty associated with the measurement may be higher than 2%. This observation when considered with the fact that 3% in stress space translates to a higher uncertainty in strain space implies that taking $\Delta > 3\%$ is a liberal definition for path dependence. Moreover, despite this liberal definition, in the sequel we will show that limit stresses are rendered path dependent.

The definition of path independence (dependence) for the XSFLC is similar to the one presented for σFLC.

4 Data of Laukonis and Ghosh: Aluminum Killed Steel

4.1 KB Model. Figure 4(*a*) presents the ϵFLCs of the as-received and the prestrained aluminum killed steel sheets from the article by Laukonis and Ghosh [3]. The level of the tensile equibiaxial engineering strain is indicated in the legend. Tensile equibiaxial prestrain is denoted by "B." Therefore, B271 implies an equibiaxial engineering prestrain of 0.271. It can be seen that the presence of prestrains shifts and distorts the shape of the limit curves when compared with the as-received curve, and the prestrained FLCs are well outside the 2% uncertainty associated with the FLC of the as-received material. That is, the presence of prestrains renders the ϵFLC for aluminum killed steel path dependent.

The KB model was used to transform the ϵFLCs into stress space, and the resulting curves are shown in Fig. 4(*b*). Equations used to obtain the stress-based FLCs are presented in Appendix C. These σFLCs compare well with those reported by Stoughton [8]. When the prestrain is 0.07, the stress-based FLC is path independent, since the difference, Δ, with respect to the as-received curve in the plane-strain region is less than 3%. By way of contrast, for prestrains greater than 0.07, the limit curves are path dependent, in that the forming limit stresses differ from the forming limit stresses of the as-received material and for path B271 by as much as 70 MPa.

The σFLCs were transformed into XSFLCs as shown in Fig. 4(*c*). Here, effective stress is given by $(\phi/2)^{1/6}$, where ϕ is given by Eq. (2). Again, for the prestrain of 0.07, the XSFLC is path independent, and for prestrains greater than 0.07, the XSFLCs are path dependent. It is interesting to note that despite applying nonlinear transformations on the σFLC to obtain the XSFLC, if the σFLC is path dependent (independent) in principal stress space, it is path dependent (independent) in XSFLC space. The path dependent XSFLC for path B271 differs from the as-received curve by approximately 50 MPa.

To assess the validity of Assumption 3, the mean stress and effective stress at the terminal point of the primary loading path are plotted as open symbols in Fig. 4(*c*). The path dependent prestrains correspond to the square (B152) and triangle (B271). In the B152 case, the effective stress at the end of the primary path is below the minimum effective stress in the as-received XSFLC, so Assumption 3 is not invoked in the XSFLC approach. Therefore, if the as-received XSLFC is used for necking predictions, the uncertainty with reference to the plane-strain region can be as high as 6%. In the highest prestrain case (B271), Assumption 3 is invoked and the effective stress at the end of the primary loading path is to within less than 5% of the value indicated in the plane-strain region of the XSFLC for path B271. That is, for some of the prestrain paths, Assumption 3 is valid to within an uncertainty of 5%. It bears emphasis that Assumption 3 is not invoked for all of the prestrain paths and for those cases that it is invoked we are attempting to quantify the uncertainty.

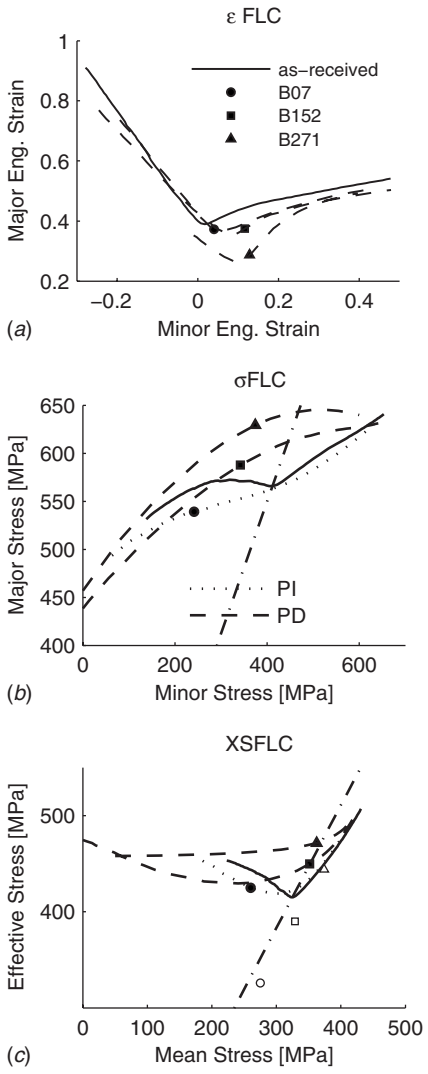

Fig. 4 (*a*) ϵFLCs from Laukonis and Ghosh [3]. (*b*) σFLCs obtained using the KB model. The dashed line denotes a path independent FLC, and the dotted lines denote path dependent ones. (*c*) XSFLCs obtained using the KB model. The open symbols are the effective stress and mean stress at the terminal point of the primary loading path. Here, effective stress is given by $(\phi/2)^{1/6}$, where ϕ is given by Eq. (2). The dashed-dotted line is the plane strain path.

4.2 BL Model. Stress-based FLCs were also obtained using the BL model and these are shown in Fig. 5. Scales in the axes of these graphs are the same as the KB model plots for steel. Model parameters a and h were obtained to be 0.67 and 0.955, respectively, and exponent m was taken to be 2. In literature, for steel, $m=6$ is recommended. It was found that $m=2$ gave the best fit, and the results can be seen in Fig. 2. The strength versus strain relationship in the RD that was used for the KB model was used for the BL model as well. The resultant stress-based FLCs are shown in Fig. 5. Effective stress, for the XSFLCs, is given by $(\phi/2)^{1/2}$, where ϕ is given by Eq. (1). The shapes of the σFLCs

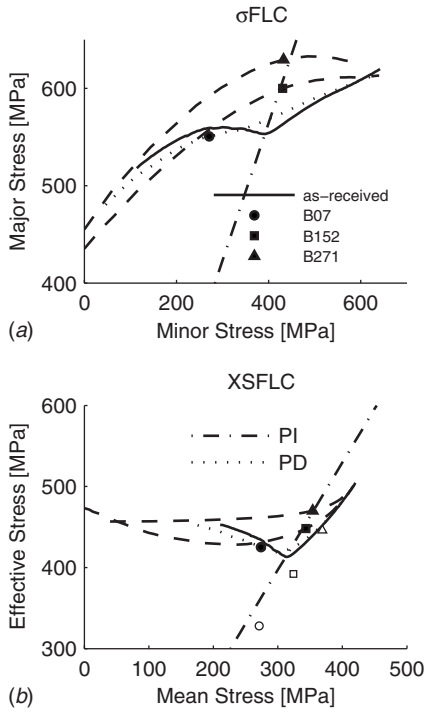

Fig. 5 (*a*) σFLCs obtained using the BL model. (*b*) XSFLCs obtained using the BL model. The effective stress is given by $(\phi/2)^{1/2}$, where ϕ is given by Eq. (1).

and XSFLCs are similar to the shapes of the curves obtained using the KB model. Those cases that were path dependent for the KB model are also path dependent for the BL model. Finally, Assumption 3 is invoked for path B271 and this assumption is valid to within an uncertainty of 5%. Assumption 3 is not invoked for path B152 and the uncertainty associated with using the as-receieved XSFLC is at most 7% with reference to the plane-strain region.

5 Al 2008-T4, Data of Graf and Hosford

In this section, analyses of Al 2008-T4 strain-based FLC data of Graf and Hosford are presented. The source data are not shown as they can be found elsewhere: Graf and Hosford [2], Stoughton [8], and Sakash et al. [10]. By way of notation, UTD17 implies primary uniaxial prestrain of 0.17 in the transverse direction. All secondary load paths, for formability assessment, were imposed in the TD, except in one data set and these are indicated, for example, as UTD05/RD, where the primary loading was uniaxial in the TD up to a prestrain of 0.05 and subsequent formability assessment was in the RD. All principal stress, effective stress, and mean stress values reported from here are in units of mega pascal.

In the formability analyses using the KB and BL models presented herein and in the sequel, there is no treatment of path independent XSFLCs. Since there is a one-to-one correspondence between principal stress pairs and the effective stress and mean stress, path independence in principal stress space implies path dependence in effective stress and mean stress space. In the interest of concision, path independent XSFLCs are not shown.

5.1 KB Model. Using the parameters for the KB model, the source ϵFLCs were transformed into stress space to obtain σFLCs and these were converted into XSFLCs; here, the definition of effective stress is $(\phi/2)^{1/8}$, where ϕ is given by Eq. (2).

Figure 6(*a*) presents the σFLCs for those experiments wherein the formability was measured in the RD after prestraining. Note that vertical axis in the graph is the principal stress in the RD. The limit curves for the as-received sheet are shown as solid lines. In all cases presented in these figures, it can be seen that path independence of the FLC is observed. Again, path independence in principal stress space translates into path independence in XSFLC space.

Figures 6(*b*) and 6(*c*) present the path independent and path dependent σFLCs, respectively, wherein the major principal direction, for formability assessment, was in the TD after prestraining; consequently, principal stress in the TD is plotted in the vertical direction. The curves have been separated based on the proposed definition of path independence. The dotted lines are used for path independence and the dashed lines for path dependence. Path dependence is observed for the higher level of prestrains in the equibiaxial and uniaxial directions.

Figure 6(*d*) presents the path dependent XSFLCs, respectively, for formability tests carried out in the TD. In the case of those limit curves that are path dependent, the path dependent effective stresses differ from the as-received ones by approximately 50 MPa. Assumption 3, which is invoked for the prestrain paths B12 (square) and B17 (diamond), is valid to within less than 5% for the former and less than 1% for the latter; this can be seen by comparing the open symbols with the corresponding filled ones in Fig. 6(*d*). For the other path dependent cases, as the effective stress at the end of prestraining is below the minimum effective stress in the as-received XSFLC, Assumption 3 is not invoked. The use of the as-received XSFLC for necking predictions in such cases results in an uncertainty as high as 5%, where, as before, the uncertainity was evaluated in the plane-strain region.

5.2 BL Model. FLCs in stress space were also obtained by using the BL model with model parameters $a=1.2$, $h=1.15$, and $m=8$, Lege et al. [26]. Figure 7(*a*) shows the σFLCs in the RD; the as-received curve is depicted with the solid line. The axes are plotted with the same scales as the KB plots for Al 2008. The shapes of these curves are different when compared with those obtained using the KB model; while the magnitudes of principal stresses and effective stresses differ by about 25 MPa and 10 MPa, respectively. Furthermore, for prestrain path UTD18/RD, the σFLC and XSFLC are path dependent (as shown by the dashed line); whereas they were path independent when the KB model was used.

Figures 7(*b*) and 7(*c*) present the path independent and path dependent σFLCs in the TD. When compared with the curves obtained using the KB model, the shapes differ, and the magnitudes of stresses are lower by approximately 35 MPa. Path dependence is observed for prestrain path B07; it was path independent when the KB model was used.

Figure 7(*d*) presents the XSLFCs. Open symbols are used to denote the effective stress and mean stress at the terminal point of the primary load path. Assumption 3 is valid to within less than 1% for path B17, and to within less than 4% for path B12. In those cases wherein the effective stress at the terminus of the primary path is lower than the lowest value of effective stress in the XSFLC, Assumption 3 is not invoked and use of the as-received XSFLC for necking prediction has associated with it an uncertainty as high as 5%.

The results of the analysis using the KB and BL models are summarized in Table 2, wherein prestrain paths, effective strain at the terminus of the prestrain path, and path independence (or dependence) are listed. Effective strains reported in the table are used in a later section. The table also lists the indication of path independence (or dependence) as per a criterion that will be presented in Sec. 7.

6 Al 6111-T4, Data of Graf and Hosford

This section presents analyses on the forming limit data for Al 6111-T4 presented in the article by Graf and Hosford [4]. In this data set, no assessment of formability was made in the RD after prestraining; all formability tests on prestrained sheet were carried out in the TD.

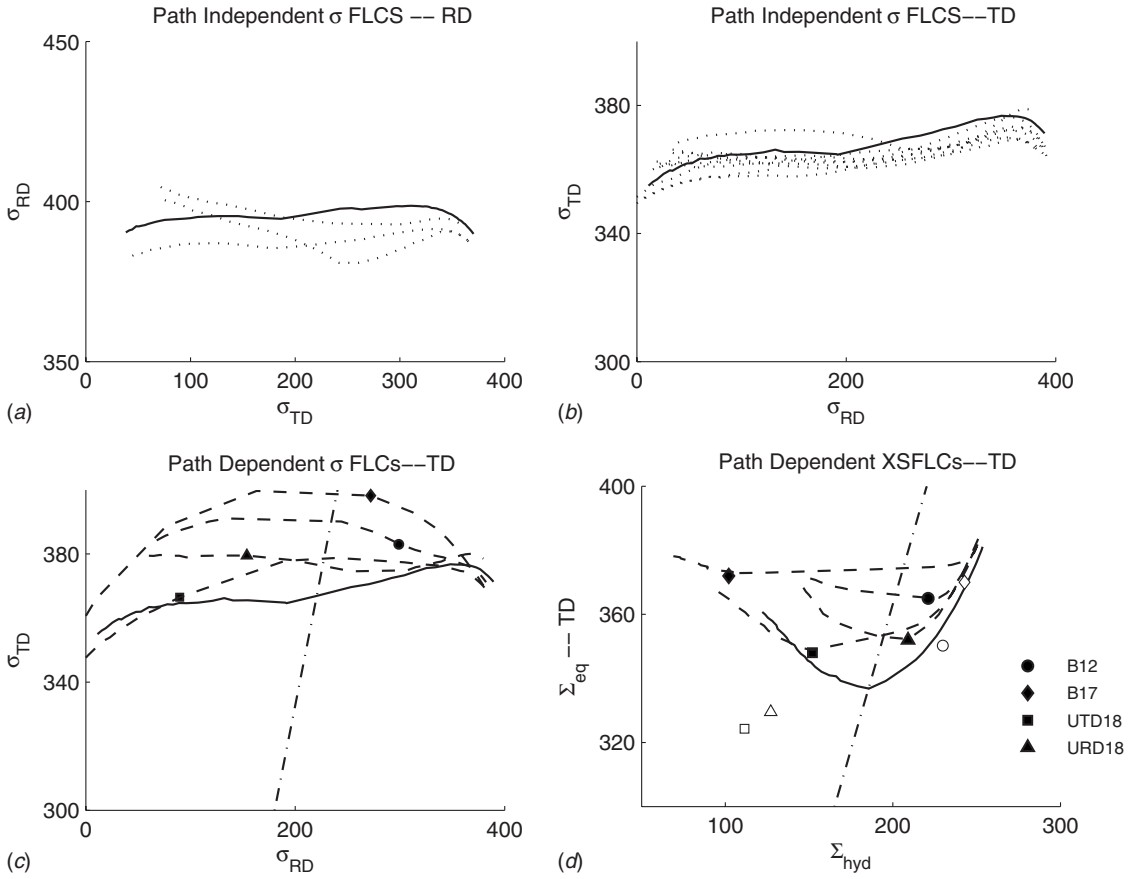

Fig. 6 Stress-based FLCs for Al 2008-T4 obtained using the formability data of Graf and Hosford [2] and the KB model. (*a*) σFLCs in the RD and (*b*) path independent σFLCs in the TD. (*c*) Path dependent σFLCs in the TD. (*d*) Path dependent XSFLCs in the TD. Open symbols in (*d*) are the values of the effective stress and mean stress at the terminus of the prestrain path. The dashed-dotted line represents the plane-strain path.

6.1 KB Model. Figures 8(*a*) and 8(*b*) present the path independent and path dependent σFLCs in the TD. Here, path dependence is observed for uniaxial, equibiaxial, and plane-strain prestrains. The plane-strain path PRD12 renders the forming limit stresses path dependent, which is in contrast to the results for Al 2008, wherein none of the plane-strain prestrains resulted in path dependence in the limit curves. Also, note that the shape is unlike those observed for Al 2008, and this is in spite of the fact that the shapes of the ϵFLCs, in the presence of prestrains, for both the materials are somewhat similar. Path dependent forming limit stresses are higher than the as-received stresses by as much as 70 MPa.

Figures 8(*d*) presents the path dependent XSFLCs. For prestrain paths B13 and B17, Assumption 3 is invoked and is valid to within less than 3% and 1%, respectively. In the other path dependent cases, Assumption 3 is not invoked, and the uncertainty associated with using the as-received curve for necking prediction is as high as 9%.

6.2 BL Model. Figure 9 presents the σFLCs in the TD obtained using the BL model with model parameters $a=1.21$ and $h=1.02$. Based on the definition of path dependence presented in Sec. 3, the σFLCs are separated into path independent (Fig. 9(*a*)) and path dependent (Fig. 9(*b*)). In contrast to the KB model, two additional prestrain load paths UTD18 and URD14 are classified as path dependent. Path dependent XSFLCs are obtained from the σFLCs and are shown in Fig. 9(*c*). Assumption 3, which is invoked for prestrain paths B085, B13, and B17, is valid to within uncertainties of 0.6%, 0.24%, and 1.4%, respectively.

Table 3 lists the results of the formability analyses using the KB and BL models.

7 Approximate Criterion for Path Dependence

In the previous three sections, analyses of the three formability data sets show that in the context of the proposed definition of path dependence the σFLCs and XSFLCs may be path dependent or path independent, and path dependence (independence) may also be a function of the constitutive model used to map the strains into stress space. These observations motivate the following question: With a knowledge of the ϵFLCs of the as-received material and the level of prestrain during the primary path, is it possible to determine whether the σFLCs and XSFLCs will display path independence (or path dependence) for a given constitutive model? In this section, this question is addressed and the next subsection presents the criterion for the aluminum killed steel data set.

7.1 Aluminum Killed Steel. Figures 10(*a*) and 10(*b*) present the basic idea of the criterion. The upper edge of the gray band is the as-received σFLC obtained using the KB (or BL) model, and the ordinates of the lower edge are 90% of those of the upper edge. The band can be viewed as enclosing a formability space. Yield contours that correspond to the effective strains at the terminus of the equibiaxial prestrain paths are shown. Those contours that overlap the gray band are shown as dashed lines and

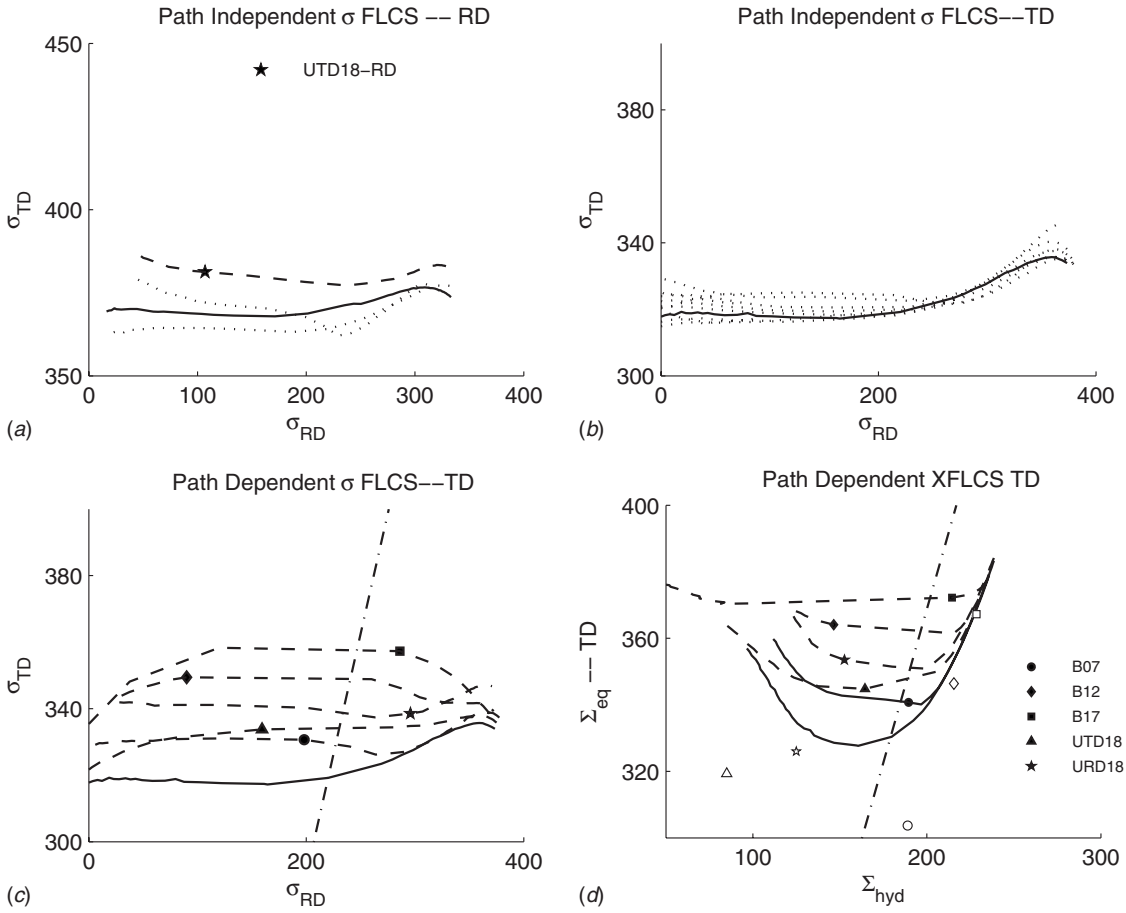

Fig. 7 Stress-based FLCs for Al 2008-T4 obtained using the formability data of Graf and Hosford [2] and the BL model. (*a*) σFLCs in the RD. UTD18/RD is path dependent in contrast to the KB model. (*b*) Path independent σFLCs and (*c*) path dependent σFLCs in the TD. (*d*) Path dependent XSFLCs in the TD. The solid lines depict as-received forming limits. The open symbols in (*d*) are the values of the effective stress and mean stress at the terminus of the prestrain path. The dashed-dotted line is the plane-strain path.

those that do not overlap are shown as dashed-dotted lines. The criterion is as follows: If there is an overlap with the gray region, path dependence in stress space is indicated. That is, path dependence is indicated for prestrain paths B152 and B271 for both models. It can be seen that this classification of σFLCs as path dependent is in agreement with the classifcation shown in Figs. 4 and 5, wherein the classification was per the definition of 3% difference (see Sec. 3). Since path dependence of the σFLC translates into path dependence of the XSFLC, the criterion can also be used to assess the path dependence of an XSLFC.

7.2 Al 2008-T4. Figure 11 presents plots of formability regions and yield contours for the Al 2008 data set. Plots are presented for both the KB model and the BL model. Horizontal gray bands, which represent the formability in the RD, were obtained as before. The right edges of the vertical bands are the as-received σFLCs in the TD, and the abscissas of the inside right edges are 90% of those of the outer right edge. The two bands can be viewed as enclosing a formability space such that when the yield contour corresponding to the prestrain falls outside the space, path dependence may be possible. Again, yield contours for effective strains (shown in Table 2) at the terminus of the primary path are plotted. Those that overlap the gray region are shown as dashed lines and the rest as dashed-dotted lines. Overlap with the gray region indicates possible path dependence of forming limits in stress space. Table 2 compares the prediction of path dependence of forming limits in stress space as obtained due to the definition of Fig. 3 with the predictions obtained using the criterion. It can be seen that in all cases, except one, the onset of path dependence predicted by the criterion is in agreement with the classification due the definition. In the case of the yield contour indicated by the filled square (PRD14), path dependence is predicted by the criterion for both the KB and BL models; whereas path independence is shown due to the classification (Figs. 6(*f*) and 7(*f*)). This discrepancy is attributed to the inaccuracies in the constitutive model.

Path UTD18/RD deserves some additional discussion. Figure 11(*c*) shows the KB model yield contour for this path (indicated by the arrow). Note that even though this yield contour, for the 18% prestrain, overlaps the vertical band, the contour is plotted as a dashed-dotted line indicating that no path dependence is predicted. The yield contour overlaps the vertical band, which represents the formability in the TD, but not the horizontal band (formability in the RD). Consequently, there is sufficient formability remaining for secondary loading of the sheet in the RD. Path independence, using the KB model, for UTD18/RD was also indicated by the definition in Sec. 3 (Fig. 6(*a*))

By way of contrast, the BL model indicated path dependence for prestrain path UTD18/RD (Fig. 7(*a*)). The yield contour for the BL model for this path, in contrast to the contour obtained from the KB model, overlaps both the vertical and horizontal bands, as shown in Fig. 11(*j*). That is, for the BL model, the criterion predicts path dependence for this FLC, which is in agreement with the classification due to the definition in Sec. 3.

7.3 Al 6111-T4. Figure 12 presents yield contours and form-

Table 2 Summary of formability analyses for Al 2008-T4 using KB and BL models. B—(tensile) equibiaxial. UTD—uniaxial stress in the TD. UT05/RD—uniaxial strain of 0.05 in the TD followed by loading in the RD. Defn.—definition. Crit.—criterion.

	$\bar{\epsilon}$		KB model		BL model	
Prestrain path	KB	BL	Defn. Fig. 3	Crit. Fig. 11	Defn. Fig. 3	Crit. Fig. 11
B04	0.077	0.073	PI	PI	PI	PI
B07	0.133	0.126	PI	PI	PD	PI
B12	0.223	0.211	PD	PD	PD	PD
B17	0.309	0.290	PD	PD	PD	PD
UTD05	0.047	0.044	PI	PI	PI	PD
UTD12	0.109	0.103	PI	PI	PI	PI
UTD18	0.160	0.151	PD	PD	PD	PD
UTD05/RD	0.047	0.048	PI	PD	PI	PI
UTD12/RD	0.109	0.110	PI	PI	PI	PI
UTD18/RD	0.160	0.160	PI	PI	PD	PD
URD04	0.04	0.035	PI	PI	PI	PI
URD125	0.121	0.116	PI	PI	PI	PI
URD18	0.170	164	PI	PI	PD	PI
PTD08	0.082	0.074	PI	PI	PI	PI
PTD13	0.130	0.118	PI	PI	PI	PI
PRD08	0.086	0.074	PI	PI	PI	PI
PRD14	0.147	0.126	PI	PD	PI	PD

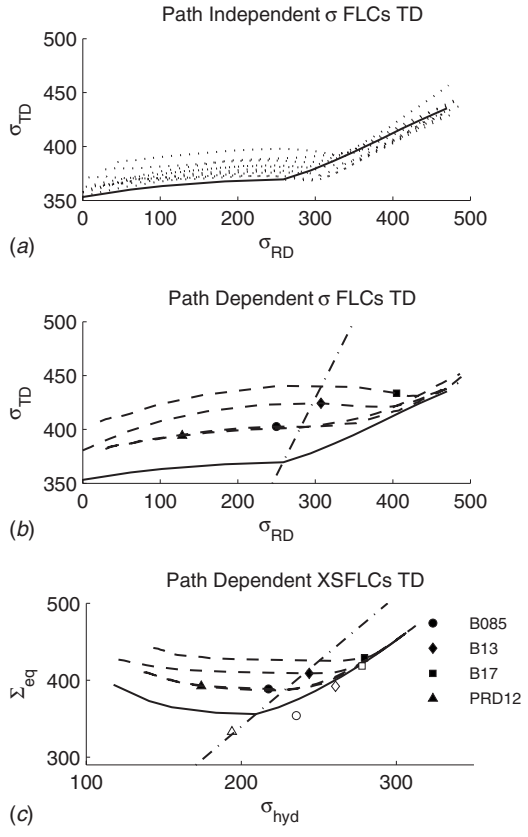

Fig. 8 Stress-based FLCs for Al 26111-T4 obtained using the data of Graf and Hosford [4] and the KB model ((*a*) and (*b*)) Path independent and path dependent σFLCs in the TD. (*c*) Path dependent XSFLCs in the TD. The solid lines depict as-received forming limits. The open symbols in (*c*) are the values of the effective stress and mean stress at the terminus of the prestrain path.

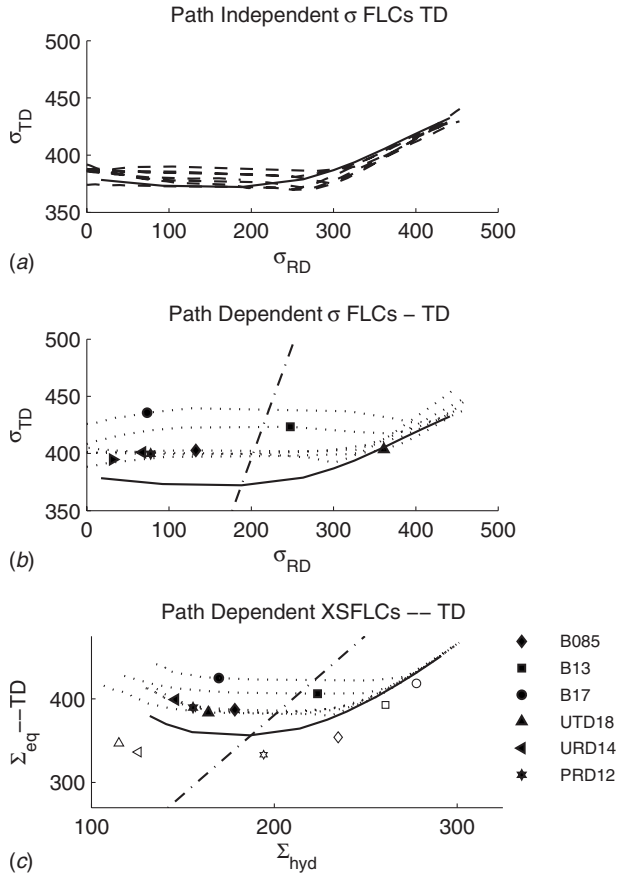

Fig. 9 Stress-based FLCs for Al 26111-T4 obtained using the data of Graf and Hosford [4] and the BL model. ((*a*) and (*b*)) Path independent and path dependent σFLCs in the TD. (*c*) Path dependent XSFLCs in the TD. The solid lines depict as-received forming limits. The open symbols in (*c*) are the values of the effective stress and mean stress at the terminus of the prestrain path.

Table 3 Summary of formability analyses for Al 6111-T4 using KB and BL models

	$\bar{\epsilon}$		KB model		BL	
Prestrain path	KB	BL	Defn. Fig. 3	Crit. Fig. 12	Defn. Fig. 3	Crit. Fig. 12
B03	0.058	0.057	PI	PI	PI	PI
B085	0.162	0.157	PD	PD	PD	PD
B13	0.243	0.236	PD	PD	PD	PD
B17	0.312	0.303	PD	PD	PD	PD
UTD05	0.058	0.047	PI	PI	PI	PI
UTD095	0.081	0.089	PI	PI	PI	PI
UTD14	0.117	0.128	PI	PI	PI	PI
UTD18	0.149	0.162	PI	PI	PD	PD
URD05	0.058	0.048	PI	PI	PI	PI
URD096	0.092	0.090	PI	PI	PI	PI
URD14	0.131	0.129	PI	PI	PD	PI
PTD05	0.050	0.050	PI	PI	PI	PI
PTD11	0.108	0.108	PI	PI	PI	PI
PRD05	0.054	0.050	PI	PI	PI	PI
PRD12	0.126	0.118	PD	PI	PD	PI

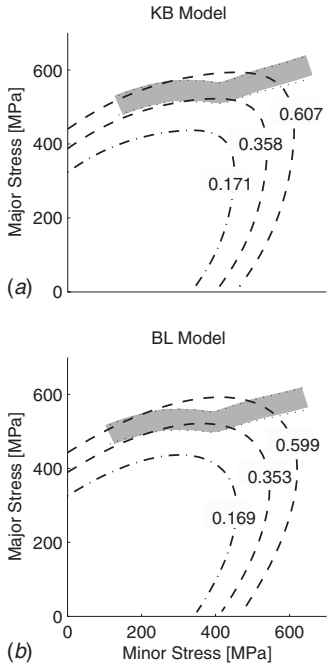

Fig. 10 Criterion for path dependency. (*a*) KB model. The upper edge of the gray band is the as-received forming limit obtained using the KB model, and the ordinates of lower edge are 90% of that of the as-received curve. Effective strains and yield contours at the terminus of the primary paths are also shown. Contours that overlap with the gray band are shown as dashed lines, and this overlap indicates possible path dependence. (*b*) BL model.

ability regions obtained using the KB and BL models for Al 6111-T4. Based on the overlap of the yield contours with the gray bands, path dependence (or independence) is classified and the path dependent ones are plotted as dashed lines. Table 3 summarizes classifications due to the criterion and the definition. First, consider the results obtained by using the KB model. Predictions using the criterion agree with those classifications obtained using the definition except for one case. For path PRD12, the criterion predicts no path dependence (as indicated by the filled square in Fig. 12(*e*)); whereas the classification due to the definition indicates path dependence (Fig. 8(*b*)). Again, this discrepancy is attributed to inaccuracies in the calibration of the constitutive model.

Next, consider the results obtained from BL model shown in Fig. 12(2). The onset of path dependence as predicted by the criterion is in accord with those obtained using the definition, with the exception of paths URD14 and PRD12 (Fig. 12(*e*)), and this contour is highlighted with a filled square. Indication of path dependence (path independence) using the criterion and the definition are also presented in Table 3.

In passing, it is worth noting that for a given constitutive model the predictions due to the proposed criterion are in good agreement with the classifications obtained using the definition of path dependence (Sec. 3).

8 Conclusions

In this article, stress-based formability limits were obtained from the strain-based formability data sets of Laukonis and Ghosh [3], Graf and Hosford [2], and Graf and Hosford [2] by using anisotropic constitutive models and isotropic hardening. The analysis showed that the magnitude and shape of the stress-based formability limits were dependent on the constitutive model used to obtained the forming limit stresses. These results are in accord with those reported elsewhere: Stoughton [8] and Sakash et al. [10]. In the present work, a definition of path dependence was proposed and it was applied to three formability data sets to show that the presence of prestrains could render some of the stress-based forming limits path dependent. The new findings of this work are itemized below. It bears emphasis that the findings apply to both the σFLC and the XSFLC.

1. The presence of prestrains may render the forming limit stresses path dependent. Forming limit stresses that correspond to the as-received ϵFLC may not be indicative of the forming limits during the secondary loading path, and the greater the level of prestrain, the greater the difference between the forming limit stresses computed for the secondary path and the limit stresses of the as-received sheet.
2. Path independence (or dependence), as defined in this work, is constitutive model dependent. That is, while forming limit stresses may be path dependent for a given prestrain and constitutive model, they may not be so when the stresses are computed using a different constitutive model.
3. In the event of path dependence, the forming limit stresses are higher than those described by the as-received σFLC and the magnitude of the difference depends on the model.
4. When the forming limit stresses are path dependent, provided that the effective stress at the terminus of the prestrain path is greater than the minimum effective stress of the XSFLC, Assumption 3 is valid to within an uncertainty of less than 5%.
5. When the forming limit stresses are path dependent, and the effective stresses at the terminus of the prestrain path is lesser than the minimum effective stress of the XSFLC, Assumption 3 is not invoked and the use of the as-received XSFLC to predict necking can lead to uncertainties as high as 9%.
6. It is possible to construct a region in stress space, which when overlapped by the yield contours corresponding to the prestrain may indicate that the forming limit stresses have been rendered path dependent for that prestrain.

9 Discussion

As already emphasized, isotropic hardening was used to in the analyses carried out in the current work. In this regard, it has been argued by Stoughton [8] that the path dependence observed in forming limit stresses may be an artifact of isotropic hardening. The argument is as follows: It is well known that isotropic hardening will overestimate the level of hardening for those paths that are farthest from the prestrain path. Therefore, the farther the secondary path is from the primary one, the larger the effect of the overestimate. Alternatively, in the event of path dependence, the best agreement between the as-received limit stresses and the prestrained limit stresses will be in the region of the primary path. Therefore, the forming limit stresses computed for the secondary paths that are close to the primary path are in better agreement with the limit stresses of the as-received material; while the limit stresses for paths farther from the primary path will not be in agreement with the as-received stresses, thus, rendering these limit stresses path dependent. This point has been addressed by Stoughton [8] and there is evidence in the current work to support it.

Consider prestrain paths B12 and B17 in Fig. 6(*c*). Since the prestrain path is equibiaxial, the isotropic hardening assumption will overpredict hardening, at the terminus of the primary path, for load paths farthest from the biaxial path. When this hardening level is used in the computation of the limit stresses for secondary plane-strain and uniaxial paths, the forming limits will be overestimated, which will render these limits path dependent. This can be seen in the figure, where the disagreement between the as-received forming limits and those corresponding to paths B12 and B17 is highest at the plane-strain and uniaxial locations. However, there is good agreement in the equibiaxial region, since the hard-

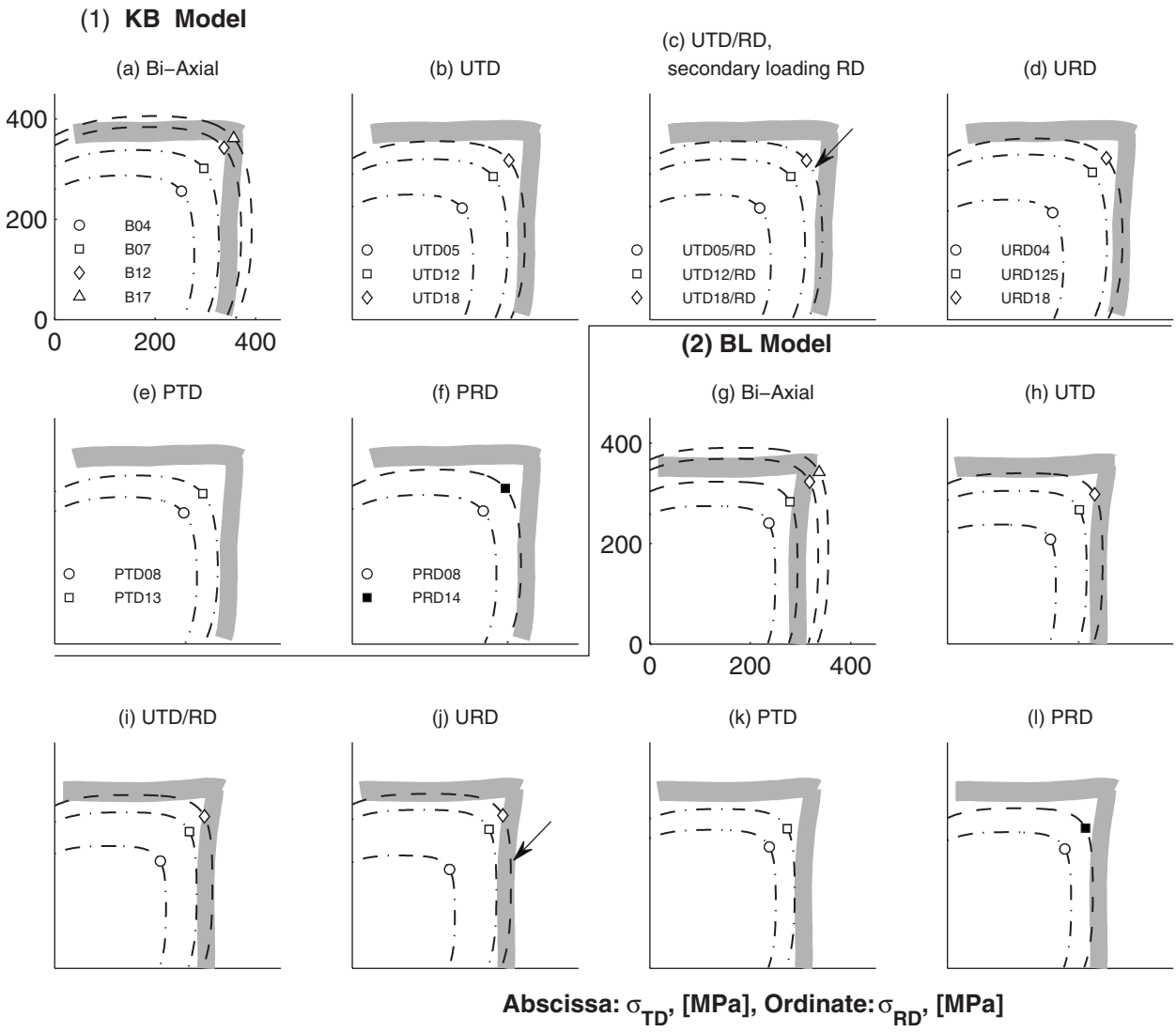

Fig. 11 Criterion for path dependency. (1) KB model. The upper edge of the gray region is the as-received forming limit in the RD obtained using the KB model, and the ordinates of lower edge are 90% of that of the as-received curve. The right edge of the gray region is the as-received forming limit in the TD, and the abscissas of the inner edge are 90% of the right edge. Effective strains and yield contours at the terminus of the primary paths are also shown. Contours that overlap with the gray band are shown as dashed lines, and this overlap indicates possible path dependence. (2) BL model. The filled symbols indicate instances where the criterion has a discrepancy with the results of Figs. 6 and 7.

ening is not overestimated in this region. Similar observations apply to the XSFLCs and σFLCS obtained using the BL model.

The foregoing arguments can also be applied to the σFLCs and XSFLCs computed for equibiaxial prestrain paths for the aluminum killed steel data and the Al 6111 data (Figs. 4, 5, 8, and 9). In all these cases, for equibiaxial prestrain paths, the best agreement between the forming limit stresses of the as-received material and the prestrained material is the right edge of the stress-based limit curves (the biaxial region is at the right edge for both the σFLC and the XSFLC).

Kinematic hardening, in contrast to isotropic hardening, where the motion of the yield surface is modeled as a function of strain as per, say, Ziegler's rule [27], will not overestimate the hardening for paths farther away from the primary path. Therefore, the forming limit stresses computed for the secondary paths that are away from the primary path may be in better agreement with the limit stresses of the as-received material. That is, use of kinematic hardening to compute the σFLCs and XSFLCs may render them path independent, or at least reduce the degree of path dependence.

There is also evidence in the current work that suggests transient hardening effects may play a role in introducing path dependence in the forming limit stresses. For Al 2008, in all of the path dependent uniaxial prestrain paths, the corresponding σFLC and XSFLC agree with the as-received curves at the uniaxial region and the equibiaxial region, but not at the plane-strain region (see Figs. 6(*c*) and 6(*d*) for the KB model; and Figs. 7(*c*) and 7(*d*) for the BL model). It is well known that for prestrained sheets the highest formability during secondary loading is along the equibiaxial path. Following reyielding during biaxial loading, transient hardening effects come into play and there is more time (because of the higher formability) for the response to transition to isotropic hardening response of the as-received condition.

Thus, kinematic and transient hardening effects play a role and introduce path dependency in forming limit stresses. In order to investigate these issues more thoroughly, what is needed are formability data sets (such as the ones analyzed in this work) and stress-strain curves measured under nonproportional loading conditions. It is worth pointing out that most nonproportional loading

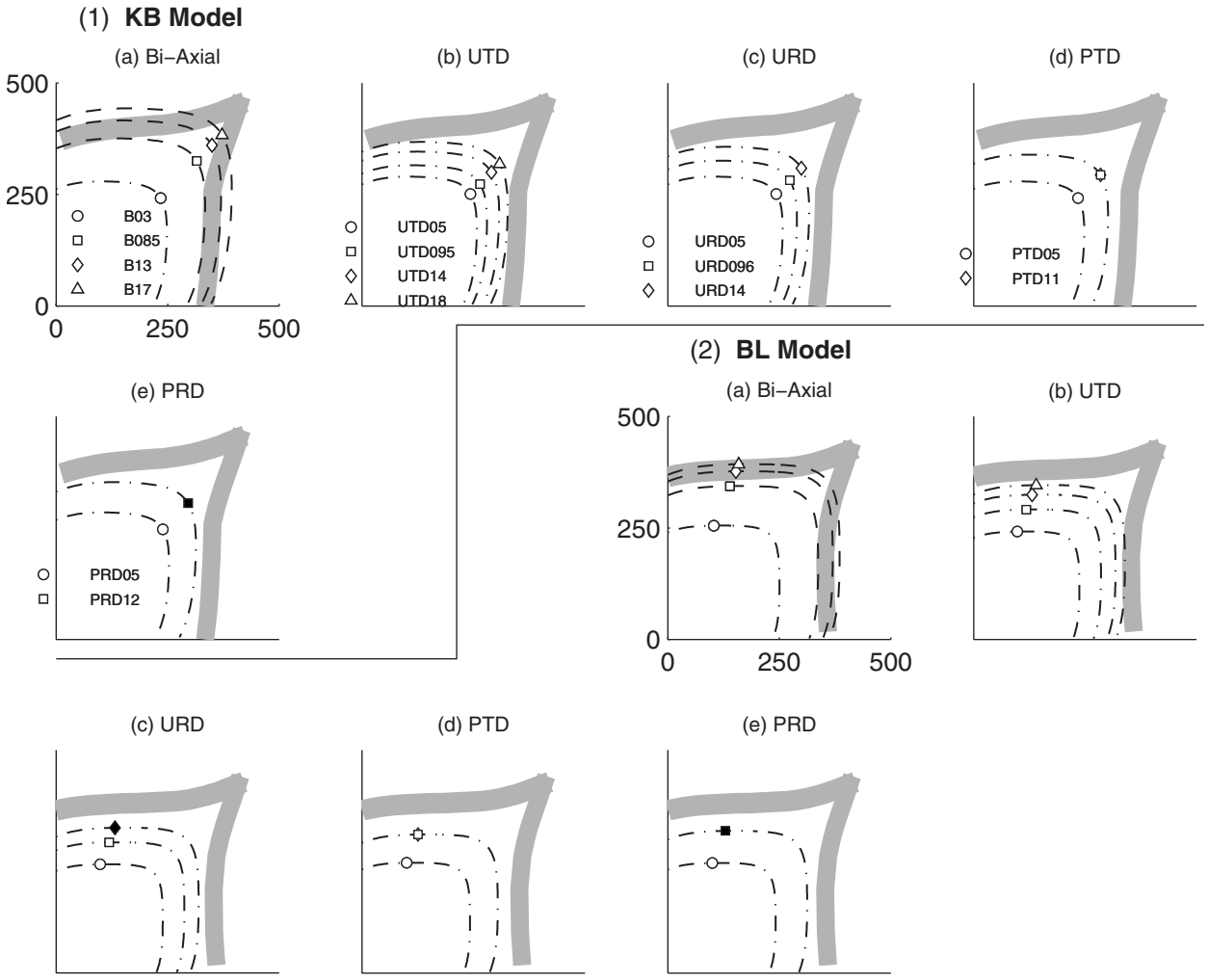

Fig. 12 Criterion for path dependency. (1) KB model. The tray region for Al6111-T4 is obtained as before. (2) BL Model. The filled symbols denote instances where the criterion has a discrepancy with the results of Figs. 8 and 9.

data are for compress-tension (or tension-compression) load paths (see, for example, Lee et al. [28]). What is needed are data for nonproportional tension-tension paths.

From the present work, it is clear that despite the path dependence observed in some instances the stress-based forming limit stresses are superior to the strain-based limit curves for predicting necking. In practice, isotropic hardening is the most widely used assumption, and, in this regard, the present work provides some assessment of the uncertainties incurred in using σFLCs and XS-FLCs for necking prediction.

Appendix A: KB Model Equations for In-Plane Loading of Sheet Metal

Let $\boldsymbol{\sigma}$ be the stress on the sheet and let $\boldsymbol{D}^p$ be the symmetric part of the velocity gradient. For plane stress loading of the anisotropic body, the IPE deviatoric stress tensor and the deformation tensor, in Voigt notation, are given by

$$\begin{Bmatrix} S_X \\ S_Y \\ S_Z \\ 0 \\ 0 \\ S_{XY} \end{Bmatrix} = \begin{pmatrix} L_{11} & L_{12} & L_{13} & 0 & 0 & 0 \\ L_{12} & L_{22} & L_{23} & 0 & 0 & 0 \\ L_{13} & L_{23} & L_{33} & 0 & 0 & 0 \\ 0 & 0 & 0 & L_{44} & 0 & 0 \\ 0 & 0 & 0 & 0 & L_{55} & 0 \\ 0 & 0 & 0 & 0 & 0 & L_{66} \end{pmatrix} \begin{Bmatrix} \sigma_x - B_1 \\ \sigma_y - B_2 \\ -B_3 \\ 0 \\ 0 \\ \sigma_{xy} \end{Bmatrix} \tag{A1}$$

$$\begin{Bmatrix} D_x \\ D_y \\ D_z \\ 0 \\ 0 \\ D_{xy} \end{Bmatrix} = \begin{pmatrix} L_{11} & L_{12} & L_{13} & 0 & 0 & 0 \\ L_{12} & L_{22} & L_{23} & 0 & 0 & 0 \\ L_{13} & L_{23} & L_{33} & 0 & 0 & 0 \\ 0 & 0 & 0 & L_{44} & 0 & 0 \\ 0 & 0 & 0 & 0 & L_{55} & 0 \\ 0 & 0 & 0 & 0 & 0 & L_{66} \end{pmatrix} \begin{Bmatrix} d_X \\ d_Y \\ d_Z \\ 0 \\ 0 \\ d_{XY} \end{Bmatrix} \tag{A2}$$

where the directions in the isotropic body are designated as X, Y, and Z. These directions are distinct from x, y, and z, which are for the anisotropic body. Furthermore, the symmetry of $\boldsymbol{L}$ and the fact that ϕ does not depend on mean stress give

$$L_{12} = \frac{L_{33} - L_{22} - L_{11}}{2}$$

$$L_{13} = \frac{L_{22} - L_{33} - L_{11}}{2}$$

$$L_{23} = \frac{L_{11} - L_{22} - L_{33}}{2}$$

$$B_3 = -B_1 - B_2 \tag{A3}$$

The principal values of $\boldsymbol{S}$ are given by

$$S_1 = \tfrac{1}{2}(S_X + S_y + \sqrt{S_X^2 + S_Y^2 - 2S_X S_Y + 4S_{XY}^2})$$

$$S_2 = \tfrac{1}{2}(S_X + S_y - \sqrt{S_X^2 + S_Y^2 - 2S_XS_Y + 4S_{XY}^2})$$

$$S_3 = S_Z \tag{A4}$$

Using the chain rule in Eq. (3) gives the symmetric part of the velocity gradient of the isotropic body as

$$d_X^p = d\lambda \frac{\partial \phi}{\partial S_X} = d\lambda \left[\frac{\partial \phi}{\partial S_1}\frac{\partial S_1}{\partial S_X} + \frac{\partial \phi}{\partial S_2}\frac{\partial S_2}{\partial S_X} + \frac{\partial \phi}{\partial S_3}\frac{\partial S_3}{\partial S_X} \right]$$

$$d_{XY}^p = \frac{d\lambda}{2}\frac{\partial \phi}{\partial S_{XY}} = \frac{d\lambda}{2}\left[\frac{\partial \phi}{\partial S_1}\frac{\partial S_1}{\partial S_{XY}} + \frac{\partial \phi}{\partial S_2}\frac{\partial S_2}{\partial S_{XY}} + \frac{\partial \phi}{\partial S_3}\frac{\partial S_3}{\partial S_{XY}} \right] \tag{A5}$$

A similar equation can be written for d_Y^p and $d_Z^p = -d_Y^p - d_X^p$ as a consequence of incompressibility. The symmetric part of the velocity gradient for the anisotropic body is obtained by the transformation $\boldsymbol{D}^p = \boldsymbol{L}\ \boldsymbol{d}^p$.

Appendix B: Model Calibration

For plane-stress loading, there are four components of $\boldsymbol{L}$ that are independent: L_{11}, L_{22}, L_{33}, and L_{66}. Components L_{44} and L_{55} are irrelevant for plane-stress loading. Tensor $\boldsymbol{B}$ has two independent components: B_1 and B_2. In addition, there are three other parameters in the yield function: m, c, and $\bar{Y}$. For the purpose of model calibration, $\bar{Y}$ is taken to be the hardening response in the RD.

To calibrate components of $\boldsymbol{L}$ and $\boldsymbol{B}$, measurements of strength at three angles to the RD, σ_0, σ_{45}, and σ_{90}, and the Lankford coefficients, R_0, R_{45}, and R_{90}, were used. Below, the procedure used for computing the model parameters is described.

Consider the primed axes, which are rotated, such that x' is at an angle θ to the RD x. When the sample is loaded in the x' direction, the strength is σ_θ, which can be transformed to the sample axis as follows:

$$\sigma_x = \sigma_\theta \cos^2\theta, \quad \sigma_y = \sigma_\theta \sin^2\theta, \quad \text{and} \quad \sigma_{xy} = \tfrac{1}{2}\sigma_\theta \sin 2\theta \tag{B1}$$

Set $\sigma_\theta = \sigma_{45}$ and obtain the stresses in the sample axes x and y using the transformation equations; then, $\boldsymbol{\sigma}$ is known. Applying the transformation tensor $\boldsymbol{L}$ on $\boldsymbol{\sigma}$ obtains $\boldsymbol{S}$. Then, the principal values of $\boldsymbol{S}$ are computed and these values are substituted into ϕ. The foregoing provides one equation relating components of $\boldsymbol{L}$ and $\boldsymbol{B}$ with σ_{45}; similarly, two more equations can be obtained for σ_0 and σ_{90}.

Next, the use of the Lankford coefficients in the model calibration is described. Returning to the primed coordinate system, the R parameter for uniaxial loading at an angle θ to the RD is

$$R_\theta = \frac{D_x^p \cos^2\theta + D_y^p \sin^2\theta - D_{xy}^p \sin 2\theta}{D_z^p} \tag{B2}$$

Using $\boldsymbol{D} = \boldsymbol{L}\ \boldsymbol{d}$ and equations (A5) and (B2), one can relate R_θ to the components of $\boldsymbol{L}$. Thus, three equations for R_0, R_{45}, and R_{90} can be obtained.

The exponent m was taken to be 8 for fcc material and 6 for bcc as per the suggestion of Hosford [22]. The parameter c is between zero and unity and a value is assumed. The six equations that relate the yield strengths and Lankford coefficients and the six unknowns in $\boldsymbol{L}$ and $\boldsymbol{B}$ are solved. The computed values of $\boldsymbol{L}$ and $\boldsymbol{B}$ are used to predict the values of yield and the R parameters at various angles to the RD. If the predicted values do not agree with the data, a new value of c is taken and $\boldsymbol{L}$ and $\boldsymbol{B}$ are recomputed. The process is repeated till a best fit to data is obtained. The foregoing process was implemented in the symbolic manipulation software MAPLE [29].

Appendix C: Equations for Computing the σFLCs-KB Model

For in-plane loading in the principal stress frame, $\sigma_{xy}=0$, and therefore, $S_{XY}=0$. In the transformation equation $\boldsymbol{D}^p = \boldsymbol{L}\ \boldsymbol{d}^p$, without loss of generality, the symmetric part of the deformation gradient can be replaced with the incremental strain tensor. That is, $d\boldsymbol{E} = \boldsymbol{L}\ d\boldsymbol{\epsilon}$, where $d\boldsymbol{E}$ is the incremental strain tensor of the anisotropic body and $\boldsymbol{\epsilon}$ is the strain increment of the isotropic body. Each point on the FLC of the sheet is designated as $(\epsilon_{yf}, \epsilon_{xf})$ and the initial prestrain as $(\epsilon_{yi}, \epsilon_{xi})$, where subscript f denotes final and i denotes initial. The corresponding point in the σFLC is $(\sigma_{yf}, \sigma_{xf})$. Using the transformation equations and noticing that $dE_{XY}=0$ give

$$\epsilon_{xf} - \epsilon_{xi} = (L_{11}dE_X + L_{12}dE_Y) \tag{C1}$$

$$\epsilon_{yf} - \epsilon_{yi} = (L_{12}dE_X + L_{22}dE_Y) \tag{C2}$$

In turn, the incremental strain tensor of the isotropic body can be written, using the associated flow rule, as

$$dE_X = d\lambda\left(\frac{cm3^m}{2^{m-1}+1}|S_X|S_X^{m-1} + m(1-c)[|S_X - S_Y|(S_X - S_Y)^{m-1} - |S_Z - S_X|(S_Z - S_X)^{m-1}] \right)$$

$$dE_Y = d\lambda\left(\frac{cm3^m}{2^{m-1}+1}|S_Y|S_Y^{m-1} + m(1-c)[|S_Y - S_Z|(S_Y - S_Z)^{m-1} - |S_X - S_Y|(S_X - S_Y)^{m-1}] \right)$$

Setting $\sigma_{xy}=S_{XY}=0$ in Eq. (A1) provides equations relating S_X, S_Y and σ_{xf}, σ_{yf}. These are substituted into the expressions for dE_X and dE_Y, which in turn are substituted into Eqs. (C1) and (C2). Thus, two equations relating $(\epsilon_{yf}, \epsilon_{xf})$ and $(\sigma_{yf}, \sigma_{xf})$ are obtained.

Furthermore, the hardening relationship and dissipation of plastic work provide

$$\bar{Y} = f(\bar{\epsilon}) \tag{C3}$$

$$\bar{Y}(\bar{\epsilon}_f - \bar{\epsilon}_i) = \sigma_{xf}(\epsilon_{xf} - \epsilon_{xi}) + \sigma_{yf}(\epsilon_{yf} - \epsilon_{yi}) \tag{C4}$$

where $\bar{\epsilon}$ is the effective plastic strain. In order to solve for the final stress state, there are four unknowns: σ_{xf}, σ_{yf}, $d\lambda$, and $\bar{\epsilon}_f$. The four equations, Eqs. (C1)–(C4), are solved simultaneously using the nonlinear solver in MAPLE.

In some of the reported data, there is a uniaxial prestrain in the RD, ϵ_{xi}; the prestrain in the TD is given by $\epsilon_{yi} = -\epsilon_{xi}R_0/(1+R_0)$. Likewise, when the initial strain is in the TD, the initial strain in the RD is $\epsilon_{xi} = -\epsilon_{yi}R_{90}/(1+R_{90})$.

References

[1] Keeler, S. P., and Backofen, W. A., 1963, "Plastic Instability and Fracture in Sheets Stretched Over Rigid Punches," ASM Trans. Q., **56**, pp. 25–48.

[2] Graf, A., and Hosford, W., 1993, "Effect of Changing Strain Paths on Forming Limit Diagrams of Al 2008-T4," Metall. Trans. A, **24A**, pp. 2503–2512.

[3] Laukonis, J. V., and Ghosh, A. K., 1978, "Effects of Strain Path Changes on the Formability of Sheet Metals," Metall. Trans. A, **9**(12), pp. 1849–1856.

[4] Graf, A., and Hosford, W., 1994, "The Influence of Strain-Path Changes on Forming Limit Diagrams of Al 6111 T4," Int. J. Mech. Sci., **36**(10), pp. 897–910.

[5] Arrieux, R., 1995, "Determination and Use of the Forming Limit Stress Diagrams in Sheet Metal Forming," J. Mater. Process. Technol., **53**(1–2), pp. 47–56.

[6] Gronostajski, I., 1984, "Sheet Metal Forming Limits for Complex Strain Paths," J. Mech. Work. Technol., **10**, pp. 349–362.

[7] Embury, J. D., and LeRoy, G. H., 1977, "Failure Maps Applied to Metal Deformation Processes," in *Advances in Research on the Strength and Fracture of Materials*, Pergamon, New York.

[8] Stoughton, T. B., 2000, "A General Forming Limit Criterion for Sheet Metal Forming," Int. J. Mech. Sci., **42**, pp. 1–27.

[9] Stoughton, T. B., 2001, "Stress-Based Forming Limits in Sheet-Metal Forming," ASME J. Eng. Mater. Technol., **123**(4), pp. 417–422.
[10] Sakash, A., Moondra, S., and Kinsey, B. L., 2006, "Effect of Yield Criterion on Numerical Simulation Results Using a Stress-Based Failure Criterion," ASME J. Eng. Mater. Technol., **128**(3), pp. 436–444.
[11] Stoughton, T. B., and Zhu, X., 2004, "Review of Theoretical Models of the Strain-Based FLD and Their Relevance to the Stress-Based FLD," Int. J. Plast., **20**(8–9), pp. 1463–1486.
[12] Yoshida, K., Kuwabara, T., and Kuroda, M., 2007, "Path Dependence of the Forming Limit Stresses in a Sheet Metal," Int. J. Plast., **23**(3), pp. 361–384.
[13] Chow, C. L., and Yang, X. J., 2003, "Prediction of Forming Limit Diagrams With Mixed Anisotropic Kinematic-Isotropic Hardening Plastic Constitutive Model Based on Stress Criteria," J. Mater. Process. Technol., **133**(3), pp. 304–310.
[14] Wu, P. D., Graf, A., MacEwen, S. R., Lloyd, D. J., Jain, M., and Neale, K. W., 2005, "On Forming Limit Stress Diagram Analysis," Int. J. Solids Struct., **42**(8), pp. 2225–2241.
[15] Marciniak, Z., and Kuczynski, K., 1967, "Limit Strains in the Processes of Stretch-Forming Sheet Metal," Int. J. Mech. Sci., **9**, pp. 609–620.
[16] Stoughton, T., and Yoon, J., 2005, "Sheet Metal Formability Analysis for Anisotropic Materials Under Non-Proportional Loading," Int. J. Mech. Sci., **47**(12), pp. 1972–2002.
[17] Simha, C. H. M., Gholipour, J., Bardelcik, A., and Worswick, M. J., 2007, "Prediction of Necking in Tubular Hydroforming Using an Extended Stress-Based FLC," ASME J. Eng. Mater. Technol., **129**(1), pp. 36–47.
[18] Simha, C. H. M., Grantab, R., and Worswick, M. J., 2007, "Application of an Extended Stress-Based Forming Limit Curve to Predict Necking in Stretch Flange Forming," ASME J. Manuf. Sci. Eng., in press.
[19] Yoshida, K., Kuwabara, T., and Kuroda, M., 2005, "Forming Limit Stresses of Sheet Metal Under Proportional and Combined Loadings," AIP Conf. Proc., **778**, pp. 478–483.
[20] Simha, C. H. M., Grantab, R., and Worswick, M. J., 2007, "Computational Analysis of Stress-Based Forming Limits," Int. J. Solids Struct., **44**(25-26), pp. 8663–8684.
[21] Barlat, F., and Lian, J., 1989, "Plastic Behavior and Stretchability of Sheet Metals 1. A Yield Function for Orthotropic Sheets Under Plane-Stress Conditions," Int. J. Plast., **5**(1), pp. 51–66.
[22] Hosford, W. F., 1972, "Generalized Isotropic Yield Criterion," ASME J. Appl. Mech., **39**(2), pp. 607–609.
[23] Karafillis, A. P., and Boyce, M. C., 1993, "A General Anisotropic Yield Criterion Using Bounds and a Transformation Weighting Tensor," J. Mech. Phys. Solids, **41**(12), pp. 1859–1886.
[24] Cao, J., Yao, H., Karafillis, A., and Boyce, M. C., 2000, "Prediction of Localized Thinning in Sheet Metal Using a General Anisotropic Yield Criterion," Int. J. Plast., **16**(9), pp. 1105–1129.
[25] Koc, M., Aue-u-lan, Y., and Altan, T., 2001, "On the Characteristics of Tubular Materials for Hydroforming Experimentation and Analysis," Int. J. Mach. Tools Manuf., **41**(5), pp. 761–772.
[26] Lege, D., Barlat, F., and Brem, J., 1989, "Characterization and Modeling of the Mechanical Behavior and Formability of a 2008-T4 Sheet Sample," Int. J. Mech. Sci., **31**(7), pp. 549–563.
[27] Khan, A. S., and Huang, S., 1995, *Continuum Theory of Plasticity*, Wiley, New York.
[28] Lee, M.-G., Kim, D., Kim, C., and Wenner, M. L., Wagoner, R. H., and Chung, K., 2005, "Springback Evaluation of Automotive Sheets Based on Isotropic-Kinematic Hardening Laws and Non-Quadratic Anisotropic Yield Functions: Part II: Characterization of Material Properties," Int. J. Plast., **21**(5), pp. 883–914.
[29] *Maple Users Guide* Version 10, 2006, Maplesoft, Waterloo, ON, Canada.